Environmental Science & Technology

Article

pubs.acs.org/est

(Micro)spectroscopic Analyses of Particle Size Dependence on Arsenic Distribution and Speciation in Mine Wastes

C. S. Kim,[†,*] C. Chi,[†] S. R. Miller,[†] R. A. Rosales,[†] E. S. Sugihara,[†] J. Akau,[†] J. J. Rytuba,[‡] and S. M. Webb[§]

[†]School of Earth and Environmental Sciences, Schmid College of Science and Technology, Chapman University, One University Drive, Orange, California 92866, United States

[‡]U.S. Geological Survey, 345 Middlefield Road, MS 901, Menlo Park, California 94305, United States

[§]Stanford Synchrotron Radiation Lightsource, 2575 Sand Hill Road, MS: 69, Menlo Park, California 94025, United States

Supporting Information

ABSTRACT: The chemical speciation and distribution of potentially toxic metal(loid)s in mine wastes is critical to assessing the risks posed by these wastes and predicting the potential bioavailability of the metal(loid)s present. Of additional potential importance is the role of particle size in the fate, transport, and toxicity of contaminated mining materials. Spectroscopic analyses of size-separated mine tailings and adjacent background samples from the Randsburg Historic Mining District, California were conducted to quantify the speciation and distribution of arsenic (As) as a function of particle size. Micro-X-ray fluorescence (μXRF) mapping of separate size fractions was used to identify multiple populations of particles with different As:Fe ratios, indicating a variety of distinct arsenic-bearing species. Bulk extended X-ray absorption fine structure (EXAFS) spectroscopy identified phases including arseniosiderite, $Ca_2Fe_3^{3+}(AsO_4)_3O_3{\cdot}3H_2O$, and As(V) sorbed to iron hydroxides (ferrihydrite, goethite), confirming a strong statistical correlation between arsenic and iron observed in both μXRF studies and bulk chemical analyses. Differences in As speciation between the mine tailings and background samples also suggest that weathering of crystalline As-bearing phases in tailings leads to sorption of dissolved arsenic to iron hydroxides in nontailings background material.

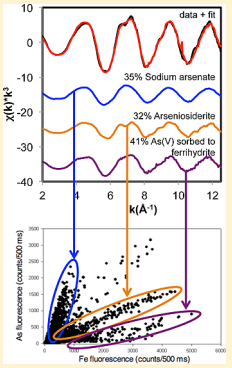

INTRODUCTION

The presence of toxic metals and metalloids in mine-impacted environments often poses an ongoing hazard to local communities long after mining operations have ceased due to the large volumes of processed mine tailings left in exposed piles at the mine sites. The possible health risks presented by mine wastes can be assessed using a variety of factors including the absolute concentrations of toxic metal(loid)s present; the potential for weathering, dispersal, and transport of the materials; and the proximity and density of human populations living near the mine wastes. Regulatory agencies commonly use these indicators to prioritize the remediation of mine wastes at abandoned mine lands.[1] More recently, chemical speciation (i.e., the discrete phases and abundances present of a certain element) has become recognized as an important determinant of a specific metal(loid)'s potential toxicity, as different chemical forms of an element can span wide ranges of solubility, reactivity, and bioavailability.[2,3]

Another critical factor in assessing the hazard level of mine wastes, although less emphasized in regulatory policy, is particle size distribution, which plays a significant role in the transport, reactivity, and human exposure pathway of toxic metal(loid)s.[4−7] For example, particles with diameters <250 μm can adhere to the surfaces of skin and food and be subsequently ingested,[8] whereas particles <10 μm can be passively inhaled into the respiratory system.[8,9] A recent study by Smith et al. reporting an increase in arsenic bioaccessibility with decreasing particle size highlights the relevance of particle size in assessing risk in contaminated environments.[10]

Macroscopic studies demonstrate that the concentrations of many trace metal(loid)s in mine tailings and contaminated background soils are strongly size-dependent, with an inverse relationship between concentration and particle size commonly observed.[11−15] Under these circumstances, metal(loid) concentrations in the finest-grained particles can exceed bulk sample concentrations by over an order of magnitude, underscoring the importance of conducting size analyses of contaminated materials instead of relying solely on bulk concentration data to formulate risk assessments. Strong statistical correlations can also often be identified between certain elements, implying that correlated elements may be chemically associated in discrete mineral or coprecipitate forms or as sorbed species onto mineral coatings.[11]

In addition to such macroscopic concentration data, information on the chemical speciation—the basis for elemental correlations—and distribution of potentially toxic metal(loid)s within samples can constrain both the anthropogenic and geochemical processes in mine-impacted environments. At the microscopic level, synchrotron X-ray techniques have proven highly useful[16−19] as they are capable of probing

Received: March 21, 2013
Revised: June 28, 2013
Accepted: July 4, 2013
Published: July 4, 2013

   dx.doi.org/10.1021/es4010653 | Environ. Sci. Technol. 2013, 47, 8164−8171

the chemical composition, association, and spatial distribution of metal(loid)s in mine wastes as a function of particle size.

In this study, microscale X-ray fluorescence (μXRF) mapping was applied to explore the distribution of arsenic and iron within size-separated mine waste and background soil samples, while bulk extended X-ray absorption fine structure (EXAFS) spectroscopy was used to identify the chemical speciation of arsenic in the same size-fractionated samples. The combination of synchrotron-based methods with corresponding macroscopic data allows differentiation between the two sample types and probes changes in metal(loid) concentration and speciation as a function of particle size, thus improving the ability to assess the mobility, exposure, and bioavailability of toxic metal(loid)s in mine wastes.

EXPERIMENTAL METHOD

Bulk grab samples were collected from mine tailings piles at the Descarga tailings dam (D-MT) and Solomon Mine (SM-MT) in the Randsburg Historic Mining District, south-central California, as well as "background" samples (SM-BG, D-BG) located a significant distance (1.4−2.6 km) from the tailings piles (see an earlier study[11] for map and other sampling details). In addition to the gold and silver ores mined and processed in this region during the late 19th/early 20th century, elevated levels of dissolved arsenic and other metal(loid)s were transported in hydrothermal solutions before being deposited with the precious metals in quartz veins. The presence of arsenic in the form of arsenopyrite in the unprocessed ore was recently identified at these locations, posing potential human health concerns.[20,21]

Approximately 2 kg of each sample was air-dried in a fume hood for several days and agitated for 30 min using a Ro-Tap Sieve Shaker Model B (Tyler Industrial Products) outfitted with 12-inch stainless steel sieves (Gilson) manufactured to ASTM E-11 specifications. This separated the sample into 11 distinct particle size fractions (Table 1), with aliquots of size fractions weighing ≥5 g sent to ALS Chemex for acid digestion and analysis by inductively coupled plasma-mass spectrometry (ICP−MS) using a Perkin-Elmer Elan 9000 spectrometer for a suite of 49 elements including all metals and metalloids.

Table 1. Particle Size Diameter (d_p) ranges for each fraction size generated through dry sieving

size fraction	particle diameter (d_p)
S1	$d_p > 2830\ \mu$m
S2	$2830\ \mu m > d_p > 1700\ \mu$m
S3	$1700\ \mu m > d_p > 1000\ \mu$m
S4	$1000\ \mu m > d_p > 500\ \mu$m
S5	$500\ \mu m > d_p > 250\ \mu$m
S6	$250\ \mu m > d_p > 125\ \mu$m
S7	$125\ \mu m > d_p > 75\ \mu$m
S8	$75\ \mu m > d_p > 45\ \mu$m
S9	$45\ \mu m > d_p > 32\ \mu$m
S10	$32\ \mu m > d_p > 20\ \mu$m
S11	$d_p < 20\ \mu$m

Micro-X-ray Fluorescence. Selected size fractions were analyzed by μXRF mapping at beamline 2−3 of the Stanford Synchrotron Radiation Lightsource (SSRL) with Si(111) monochromator crystals tuned to 14 keV and a 2 × 2 μm^2 beam spot size. A single-element solid-state Vortex Si-drift fluorescence detector (SII Nanotechnology) detected the fluorescence from the sample as it was rastered across the X-ray beam. Additional samples were analyzed at beamline 13-ID-D of the Advanced Photon Source (APS) with the same energy and beam spot size but using a 4-element Vortex-EX Si-drift detector (SII Nanotechnology). Samples were prepared as a single layer of particles dispersed evenly onto Scotch tape. The full fluorescence spectrum was saved at each point on the map and specific fluorescence peaks identified, windowed and integrated to express the relative concentrations of elements including As, Au, Ca, Cr, Cu, Fe, Hg, K, Mn, S, Si, Ti, and Zn.

Scan areas and step sizes for the various size fractions were calculated to equalize the number of particles/map and data points/particle, allowing comparison across different size fractions. Assuming particles are roughly spherical, simple-packed, and dispersed in a single layer with ∼21.5% void space, the average particle diameter of a given size fraction was used to define a scan area that would include ∼150 particles (eq 1) and a step size defined to include ∼70 data points per particle (eq 2). Scanning parameters for each size fraction are provided in Supporting Information.

$$X = \sqrt{P\frac{\pi\left(\frac{L+U}{4}\right)^2}{1-V}} \quad (1)$$

X = length of scan side (μm)
P = number of particles
L = lower limit of particle diameter range (μm)
U = upper limit of particle diameter range (μm)
V = void space fraction of total scan area

$$S = \frac{L+U}{2}\sqrt{\frac{0.785}{D}} \quad (2)$$

S = step size (μm)
D = number of data points desired per particle
0.785 = fraction of a square that an inscribed circle occupies

Upon completion of μXRF mapping, the software program Microanalysis Toolkit[22] was used to generate element-specific fluorescence maps and correlation plots between selected pairs of elements. For all maps, maximum intensity threshold values of arsenic and iron were scaled down by 50% to increase their brightness and visibility. For samples analyzed at the APS, micro-X-ray diffraction (μXRD) was conducted on selected As- and Fe-rich particles to attempt single-particle phase identification. This technique provided limited information which is summarized in the Supporting Information.

Extended X-ray Absorption Fine Structure (EXAFS) Spectroscopy. Bulk As K-edge EXAFS spectroscopic analysis was conducted on size fractions of all samples at beamline 11−2 at SSRL using Si(220), $\varphi = 90°$ monochromator crystals at room temperature in fluorescence mode with a Lytle detector for samples where $[As]_T > 1000$ mg/kg (ppm) and a Ge 30-element detector when $[As]_T < 1000$ ppm. Samples were pulverized using a mortar and pestle (S6 and coarser fractions only), loaded into 1.5 mm-thick Teflon holders, and sealed with Kapton tape before EXAFS spectra were collected with a 2 × 14 mm^2 beam. Aluminum filters attenuated background matrix fluorescence from the iron in the sample. Energy calibration was conducted for each scan with an As(0) foil placed downstream from the sample and by assigning the first inflection point of the foil's absorption edge to 11867.0 eV.

dx.doi.org/10.1021/es4010653 | Environ. Sci. Technol. 2013, 47, 8164−8171

The speciation of arsenic in the samples was determined by comparison of their EXAFS spectra with a subset of spectra selected from an arsenic model compound EXAFS library of homogeneous arsenic phases of variable oxidation states including crystalline, amorphous, and sorbed compounds (Figure 1). Each model EXAFS spectrum, reflecting the distinct structural arrangement of arsenic in that particular species, is unique and can therefore be utilized as a component phase in combination with other model spectra to characterize a heterogeneous, natural arsenic-bearing sample. The As EXAFS spectra of the mine waste samples were analyzed using a linear least-squares fitting method that has been employed in a range of environmental systems[23−26] to deconvolute the composite spectrum of the natural sample into the sum of its individual arsenic-bearing components. X-ray absorption spectra of both the waste samples and the model compounds were energy-calibrated using the same As(0) foil and starting E_0 value of 11887.0 eV to ensure no spurious offsets between spectra that would compromise the fitting process.

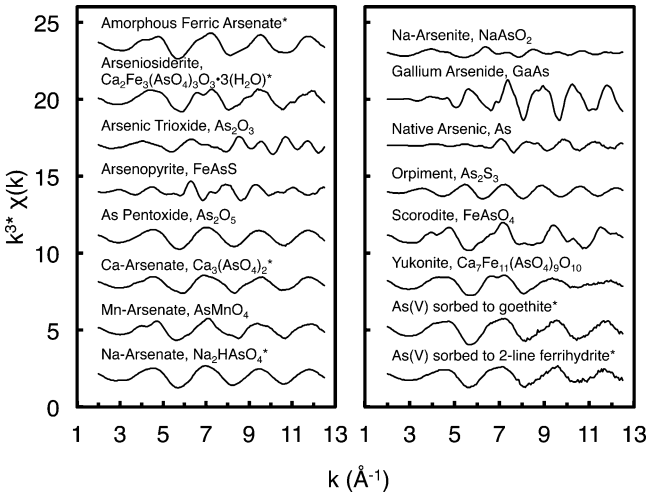

Figure 1. Arsenic model compound library composed of EXAFS spectra of homogeneous As phases including crystalline, synthetic, and sorbed compounds. Model compounds used in linear combination fitting, based on PCA and target transform analysis, are indicated with asterisks.

EXAFS spectra were averaged, background-subtracted, and fit over a k-range of 2−12.5 Å^{-1} (tailings samples) or 2−10 Å^{-1} (background samples) using the SixPack software program.[27] All experimental EXAFS spectra (a total of 27 spectra from 4 sites) were then subjected as a complete set to principal component analysis (PCA) in order to statistically determine the number of discrete unique components required to reconstruct all spectra to a 95% confidence interval.[28] The PCA results concluded that a minimum of 3 and a maximum of 5 components were necessary to sufficiently fit each spectrum in the data set. Target transform analysis was then conducted using the model compound database to identify model compound spectra that constitute probable components from the original set of unknown EXAFS spectra.[29] From this analysis, a subset of model compounds was determined and utilized for subsequent linear combination fitting, including: Na-arsenate, Ca-arsenate, amorphous ferric arsenate, arseniosiderite, and As(V) sorbed to Fe-(oxy)hydroxides (goethite and 2-line ferrihydrite, which in the results (mostly in the SI) are reported both separately and together as a single category).

Each model compound was first fitted against an experimental spectrum individually, with the compound yielding the best fit (i.e., the lowest R-factor, an indicator of fit quality) selected as the first component for subsequent fits. Additional model compound spectra were then individually combined with the first component to generate two-component fits, repeating the process until no more significant contributors, i.e., those representing ≥10% of the total fit, could be added that caused the R-factor value to decline by ≥10%. This "cycle fit" process, developed by the authors and now a permanent component of SixPack, rapidly produces both the identification of the relevant arsenic species and their percent contributions to the fit, representing the EXAFS-determined arsenic speciation of that sample. Use of EXAFS spectroscopy, while providing a direct, nondestructive route to characterizing arsenic speciation, is limited to the spectra in one's model compound database, has relatively high detection limits of ∼100 ppm $[As]_T$ [30] and is considered to have errors of ±25% of stated values in the final quantitative phase determinations based on past studies using empirical model compound mixtures.[31,32]

Shell-by-shell fitting was attempted on all samples using phase and amplitude functions from model single-shell scattering paths (e.g., As−O, As−Fe, As−As) generated in SIXPack using Feff6l.[33] Likely due to the presence of multiple As species in each sample, which would prevent clear discrimination of second-shell features, this method was not sufficiently effective at distinguishing differences between samples nor as a function of particle size.

RESULTS AND DISCUSSION

For brevity, figures in this manuscript are limited to the Descarga tailings dam (D-MT) sample, which accounts for both the largest volume of tailings and among the highest arsenic concentrations in the Randsburg mining district, thus representing the most significant environmental concern in the region. Summarized results are provided for all samples, with more details available in the SI.

Particle Size-Dependence of Arsenic and Iron Concentrations. Figure 2 shows size-dependent concentration plots for arsenic and iron in the D-MT sample, with average bulk concentrations of the elements indicated as horizontal dotted lines on each plot. Arsenic strongly shows and iron generally shows an inverse relationship between particle size and concentration; as discussed in an earlier companion

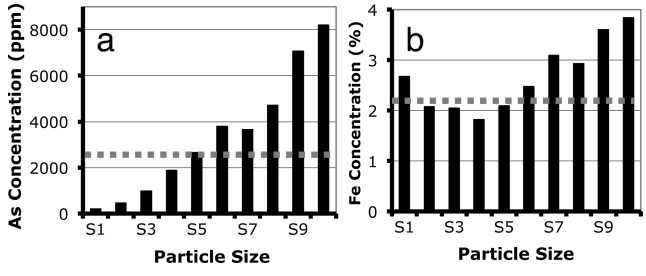

Figure 2. Arsenic (a) and iron (b) concentrations as a function of particle size in the Descarga mine tailings (D-MT). The average bulk concentration of each element is designated by a dotted gray line. Refer to Table 1 for a description of the particle size ranges corresponding to each size fraction.

dx.doi.org/10.1021/es4010653 | Environ. Sci. Technol. 2013, 47, 8164−8171

study,[11] this trend is consistent with the elements occurring in a relatively insoluble phase(s) that persists during the chemical weathering and breakdown of material relative to the other matrix phases present. If the element-bearing phase(s) additionally exhibits a low mineralogical hardness, physical weathering processes can further concentrate that element into progressively finer grain size fractions, as has been postulated for mercury in mine wastes.[12]

Alternatively, an inverse relationship would also result from the element existing as a sorbed species, e.g., As(V) sorbed to iron oxyhydroxides, where the proportion and/or surface area of the sorbing phase increases with decreasing particle size. The linear correlation coefficient (r) between arsenic and iron in the D-MT sample using the concentrations of both elements across all size fractions is 0.852 (r^2 = 0.726), indicating that the elements may be coassociated either as a sorbed species to a mineral substrate or in an As/Fe-bearing mineral. However, since [As] increases by over a factor of 40 while [Fe] increases by a factor of 2 with decreasing particle size, a fraction of arsenic likely exists independently of iron and vice versa.

Relative to the average bulk concentrations of arsenic and iron in the sample (2703 ppm and 2.25%, respectively), the finer size fractions are substantially enriched, with the S10 size fraction exceeding the bulk arsenic concentration by over 200% and the bulk iron concentration by 70% (8210 ppm and 3.84%, respectively). In the absence of such a size-dependent analysis, only bulk concentrations of contaminated samples would be compared to regulatory screening levels, underestimating the actual trace metal(loid) concentrations of the finer size fractions which are most prone to incidental ingestion and inhalation. Such an underestimate may result in incorrect assessments as to whether remediative action should be employed in an abandoned mining region.

Similar concentration trends and enrichments above bulk arsenic and iron concentrations are observed in the D-BG and SM-BG samples, whereas the SM-MT sample displays minima in both concentrations in the S5 fraction and progressively increasing concentrations with both coarser and finer particle sizes (see the SI for plots). This trend was rarely observed among many samples investigated, but may be indicative of the presence of two separate phases with opposing concentration trends; i.e., one phase may display an inverse relationship, while the other may display a direct relationship between particle size and element concentration.[11] Among all three samples, however, the correlation between arsenic and iron is very strong (r ranges from 0.901 to 0.987), further supporting chemical association(s) between the two.

μXRF Mapping. Figure 3 shows μXRF maps for the S5 (250−500 μm), S7 (75−125 μm), S9 (32−45 μm), and S11 ($\leq$20 μm) size fractions of the D-MT sample, with arsenic Kα fluorescence represented in red and iron Kα fluorescence in blue. (Maps for the D-BG, SM-MT, and SM-BG samples are included in the SI.) The approximate number of particles is generally consistent across the different maps, validating the normalization calculations presented earlier. Both reflected light images (not shown), SEM analysis,[11] and the μXRF maps from this study confirm that the size fractions consist primarily of particles in their expected size ranges and not of multiparticle aggregates or particles considerably smaller than the size range, which might result from inadequate sieving.

Among all size fractions, arsenic is nonuniformly distributed throughout the sample and can be frequently identified in concentrated discrete particles, with increasing amounts of

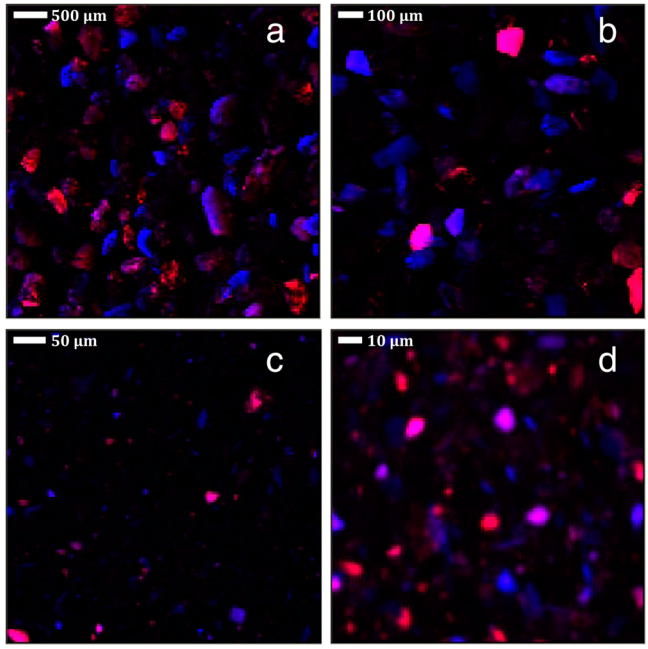

Figure 3. Micro-XRF maps of the (a) S5 (250−500 μm), (b) S7 (75−125 μm), (c) S9 (32−45 μm), and (d) S11 ($\leq$20 μm) size fractions of the D-MT sample. Arsenic Kα fluorescence = red and iron Kα fluorescence = blue. The maximum intensity threshold of both elements was scaled down by 50% to increase their brightness in the maps.

arsenic corresponding to stronger intensities of the color red within a given sample's μXRF map. Although in all size fractions arsenic and iron are visible separately (as pure red or blue particles) they are also often located together (as purple particles), supporting the positive but not exclusive correlation between arsenic and iron identified earlier. The range of purple hues indicates variable relative concentrations of arsenic and iron (i.e., As:Fe ratios) in different particles.

Scatterplots of arsenic vs iron fluorescence counts of the S5, S7, S9, and S11 maps are shown in Figure 4 and correspond directly to the maps from Figure 3. These correlation plots show that with decreasing particle size, progressively stronger positive correlations between arsenic and iron can be observed, consistent with the strong linear correlation coefficient from the bulk analyses. Multiple populations of positively correlated data points can also be identified in the scatterplots, appearing as "fingers" of points distributed along lines of constant slope. These discrete populations represent different As:Fe ratios and likely correspond to distinct minerals or phases in which both elements are present.

The plots in Figure 4 indicate that the arsenic and iron distributions are more diffuse among the larger grains and become both more localized and correlated within distinct particles (populations) with decreasing particle size. The variable extent of X-ray fluorescence emission from particles of different sizes (and potentially compositions) is also likely a contributing factor, with the scatterplots of the larger size fractions more representative of particle surfaces and those of the smaller size fractions representing more of the entire particles, allowing better resolution of distinct As:Fe ratios.

Changes in the distribution and speciation of arsenic as a function of particle size can result from: (1) the mechanical and chemical weathering of larger particles, increasing the proportion of smaller particles; (2) the increased surface

dx.doi.org/10.1021/es4010653 | Environ. Sci. Technol. 2013, 47, 8164−8171

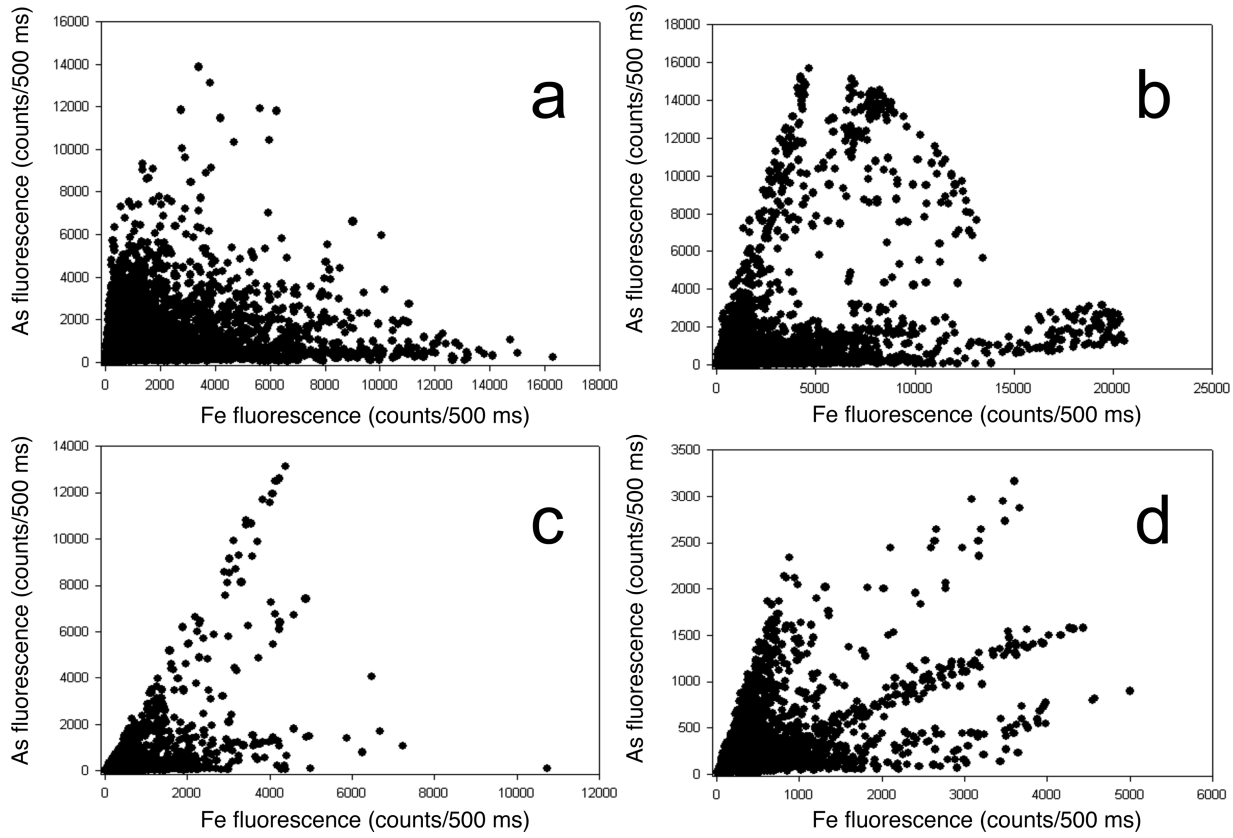

Figure 4. Iron vs arsenic correlation scatterplots of D-MT particle size fractions (a) S5 (250−500 μm), (b) S7 (75−125 μm), (c) S9 (32−45 μm), and (d) S11 (≤20 μm).

areas of smaller particles, enhancing the dissolution and secondary mineralization of primary arsenic-bearing phases or adsorption of dissolved arsenic onto iron hydroxides; and (3) the formation of primary or secondary mineralized arsenic species with small grain/crystallite sizes. Due to the excavation, stamp milling, chemical leaching, and subsequent decades of exposure which these materials have undergone, it is likely that weathering processes have played the most significant role in the current arsenic concentration and distribution trends. All samples investigated reveal similar trends of increasing localization of As−Fe species populations with decreasing particle size, consistent with weathering as the primary mechanism for such trends since it would apply comparably across different sites and different media. They also all show between 3 and 4 such populations, in agreement with PCA results and suggesting the presence of an equal number of As-bearing species.

EXAFS Spectroscopy. Figure 5 shows a representative example of an EXAFS linear combination fit result for the S11 size fraction from the Descarga mine tailings. The three components, As(V) sorbed to Fe-(oxy)hydroxides (goethite + ferrihydrite), sodium arsenate (Na_2HAsO_4), and arseniosiderite ($Ca_2Fe_3^{3+}(AsO_4)_3O_3{\cdot}3H_2O$) comprise the species identified in this sample at non-normalized proportions of 41%, 35%, and 32% respectively. The sum of the proportions (108%) and the relatively low R-factor value of 0.0132 both indicate a very good quality fit. Furthermore, all three phases are oxidized As(V) species, consistent with the oxidizing nature of the desert environment in which the tailings are located.

The identification by both EXAFS spectroscopy and μXRD (see SI) of arseniosiderite, a secondary mineral formed by the

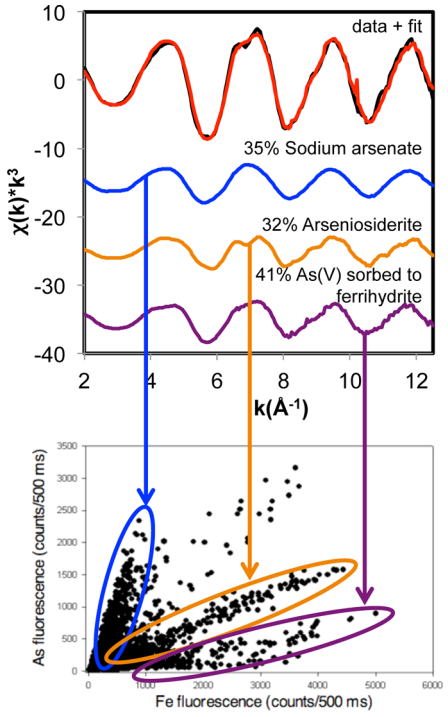

Figure 5. Linear combination fitting results for the S11 size fraction of the D-MT sample. At top is the raw EXAFS spectrum (black line) overlain by the linear combination fit (red line), followed by the three components determined to comprise the best fit. Underneath is the D-MT_S11 correlation scatterplot to show the associations between the μXRF and EXAFS speciation analyses.

dx.doi.org/10.1021/es4010653 | Environ. Sci. Technol. 2013, 47, 8164−8171

oxidation of arsenopyrite or other arsenic-bearing species,[34−37] and by EXAFS of As(V) sorbed to Fe-(oxy)hydroxides is consistent with the strong correlation between iron and arsenic observed in the macroscopic and μXRF studies. The presence of arseniosiderite also corresponds with bulk correlation coefficients between calcium and arsenic (0.718−0.986, average 0.896) but could not be readily validated through μXRF due to low fluorescence intensity and detection from calcium. Sodium arsenate, while not a naturally occurring phase, can potentially form under these anthropogenically influenced conditions through dissolution and reprecipitation as effluorescent salts; the slightly elevated levels of sodium in the tailings (1.5−1.8%) relative to the background samples (1.0−1.6%) further support the greater proportions of Na-arsenate in the former samples (SI). The identification of Na-arsenate through the restricted linear combination fitting conducted may alternatively represent any number of iron-free As(V) phases (including Mn-arsenate or arsenic pentoxide) which have similar short-range structural arrangements, as evidenced by the only slight differences in their EXAFS spectra (Figure 1).

Comparison of the EXAFS fitting with the μXRF mapping shows close agreement regarding the number and chemistry of discrete species present in the sample, with the three arsenic phases identified with EXAFS likely corresponding with the three dominant populations observed in the As:Fe correlation scatterplot of the S11 size fraction (Figures 4d and 5); a fourth population can be slightly seen but is composed of significantly fewer pixels than the other three groups, and so is likely a minimal contributor to the overall arsenic speciation and was not identified by EXAFS spectroscopy. The slopes of the three primary populations can be associated with the stoichiometric As:Fe ratios of the three identified phases, with the low, intermediate, and high slopes corresponding to the As(V) sorbed to Fe-(oxy)hydroxides (As:Fe $\ll$1), arseniosiderite (As:Fe ~1), and sodium arsenate (As:Fe$\gg$1), respectively. The nonvertical slope of the phase identified as sodium arsenate suggests that trace iron may be substituting for sodium and/or a iron-bearing phase may be physically associated in the same area (e.g., Fe-oxyhydroxide surface contamination or rinds) which contributes minor iron fluorescence to the population of pixels corresponding to sodium arsenate.

Distinct speciation differences and relationships between mine tailings and background samples can be observed in Figure 6, which plots the proportions of As(V) sorbed to Fe-(oxy)hydroxides and Na-arsenate against one another for all samples. An inverse relationship between the two phases exists among the mine tailings samples but not among the background samples, as Na-arsenate is largely absent in the background samples (but is present from 24 to 76% in the tailings). However, sorbed As(V) is more dominant in the background samples (51−93%) than the tailings samples (0−53%). Additionally, the substrate of the sorbed As(V) is more likely to be ferrihydrite in the tailings and goethite in the background samples (SI). These speciation differences are consistent with the intensive processing of arsenic-rich ore and weathering of the subsequent tailings, resulting in the dissolution of primary crystalline arsenic phases (e.g., sodium arsenate, which is highly soluble in water[38]) and the formation of poorly-/nanocrystalline ferrihydrite and secondary minerals like arseniosiderite.[39] Arsenic therefore appears to be transported to background regions primarily as secondary mineral particles or as a dissolved species which then sorbs to the more

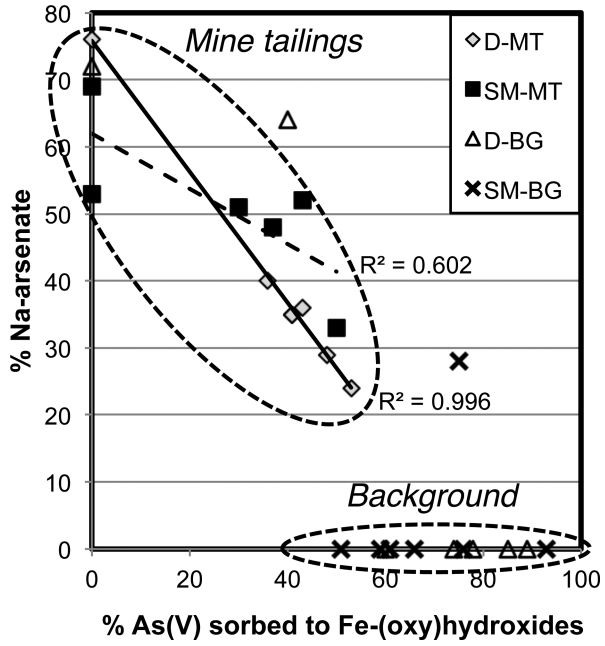

Figure 6. Correlation plot of Na-arsenate vs As(V) sorbed to Fe-(oxy)hydroxides as determined through linear combination fitting of EXAFS spectra for mine tailings and background samples. Results show clear speciation differences between the two sample categories, suggesting that weathering/dissolution of crystalline As species in the tailings results in As(V) sorption to Fe-oxyhydroxides in background regions.

crystalline Fe-oxyhydroxides (goethite) widely distributed throughout the surrounding region.

Linear combination fits of the S5−S11 size fractions generated from each sample identify one or more of the three arsenic-bearing species present in the D-MT sample (SI), but in varying proportions that do not reveal discernible speciation trends as a function of particle size. Changes in both arsenic speciation and concentration as a function of particle size can influence its bioaccessibility;[10] in addition, smaller particles have considerably greater transport properties through waterborne or windborne processes which can influence the potential for arsenic exposure among the finest-grained particles. Conversely, however, arsenic may bind more strongly to smaller particles or matrix phases that are more abundant in smaller size fractions (e.g clays, Fe-oxides), reducing their lability and potential toxicity.[40]

Although bulk arsenic concentration generally increases with decreasing particle size, arsenic speciation as determined by EXAFS spectroscopy does not change nearly as dramatically or systematically, suggesting that arsenic speciation is largely preserved across the size fractions of a given sample as observed recently when comparing airborne particles to near-surface tailings.[16] The significant role that physical weathering processes play in arsenic speciation, however, is best demonstrated by the distinct speciation differences between tailings and background samples. Also, the inverse relationship between arsenic concentration and particle size suggests that arsenic mobility is considerably enhanced since finer-grained particles are more susceptible to waterborne or airborne transport.

The combination of bulk chemical analysis, μXRF, and EXAFS spectroscopy provides a powerful approach to characterizing the distribution and speciation of selected

dx.doi.org/10.1021/es4010653 | Environ. Sci. Technol. 2013, 47, 8164−8171

elements as a function of particle size in mine waste materials. Our subsequent studies are investigating the relationship between particle size and arsenic solubility in order to correlate concentration, distribution, and speciation with the bioaccessibility of arsenic in different size fractions of contaminated mine wastes. This information can identify important trends in both the concentration and chemical composition of contaminants such as arsenic that have implications for the exposure, transport, and potential bioavailability of arsenic to communities living in the proximity of abandoned mine lands.

■ ASSOCIATED CONTENT

Supporting Information

Plots of arsenic and iron concentrations as a function of particle size; μXRD analysis of selected size fractions; μXRF maps and associated scatterplots; and EXAFS linear combination fitting results for all samples. This material is available free of charge via the Internet at http://pubs.acs.org.

■ AUTHOR INFORMATION

Corresponding Author

*E-mail: cskim@chapman.edu.

Notes

The authors declare no competing financial interest.

■ ACKNOWLEDGMENTS

We would like to acknowledge Joe Rogers (SSRL) and Matt Newville (APS) for their assistance with μXRF and EXAFS data collection. Portions of this research were carried out at the Stanford Synchrotron Radiation Lightsource, a national user facility operated by Stanford University, and at the Advanced Photon Source at Argonne National Laboratory on behalf of the U.S. Department of Energy, Office of Basic Energy Sciences. The arsenic model compounds used for linear combination fitting were generously provided by Andrea Foster of the USGS. This work was funded by the USGS Mineral Resources External Research Program (No. 06HQGR0181), an NSF-CAREER Award (No. 0847811), and a subcontract from the Bureau of Land Management. The authors wish to thank Chapman Environmental Geochemistry Laboratory members James Dale, Kevin Meston, Suzie Shdo, John Stegemeier, and Kim Wilson for their assistance with aspects of this project.

■ REFERENCES

(1) EPA, *Exposure Factors Handbook*; National Center for Environmental Assessment, Office of Research and Development, 1997.

(2) Reeder, R. J.; Schoonen, M. A. A.; Lanzirotti, A. Metal speciation and its role in bioaccessibility and bioavailability. *Med. Mineraol. Geochem.* **2006**, *64*, 59−113.

(3) Guthrie, G. D. Mineral properties and their contributions to particle toxicity. *Environ. Health Perspect.* **1997**, *105*, 1003−1011.

(4) Csavina, J.; Landazuri, A.; Wonaschuetz, A.; Rine, K.; Rheinheimer, P.; Barbaris, B.; Conant, W.; Saez, A. E.; Betterton, E. A. Metal and metalloid contaminants in atmospheric aerosols from mining operations. *Water Air Soil Pollut.* **2011**, *221* (1−4), 145−157.

(5) Juhasz, A. L.; Weber, J.; Smith, E. Impact of soil particle size and bioaccessibility on children and adult lead exposure in pen-urban contaminated soils. *J. Hazard. Mater.* **2011**, *186* (2−3), 1870−1879.

(6) Schaider, L. A.; Senn, D. B.; Brabander, D. J.; McCarthy, K. D.; Shine, J. P. Characterization of zinc, lead, and cadmium in mine waste: Implications for transport, exposure, and bioavailability. *Environ. Sci. Technol.* **2007**, *41* (11), 4164−4171.

(7) Momani, K. A. Partitioning of lead in urban street dust based on the particle size distribution and chemical environments. *Soil Sed. Contam.* **2006**, *15* (2), 131−146.

(8) Plumlee, G. S.; Ziegler, T. L., The Medical Geochemistry of Dusts, Soils, and Other Earth Materials. In *Treatise on Geochemistry*; Elsevier: New York, 2003; Vol. *9*, pp 263−310.

(9) Plumlee, G. S.; Morman, S. A.; Ziegler, T. L. The toxicological geochemistry of earth materials: An overview of processes and the interdisciplinary methods used to understand them. *Med. Mineral. Geochem.* **2006**, *64*, 5−57.

(10) Smith, E.; Weber, J.; Juhasz, A. L. Arsenic distribution and bioaccessibility across particle fractions in historically contaminated soils. *Environ. Geochem. Health* **2009**, *31*, 85−92.

(11) Kim, C. S.; Wilson, K. M.; Rytuba, J. J. Particle-size dependence on metal(loid) distributions in mine wastes: implications for water contamination and human exposure. *Appl. Geochem.* **2011**, *26* (4), 484−495.

(12) Kim, C. S.; Rytuba, J. J.; Brown, G. E., Jr. Geological and anthropogenic factors influencing mercury speciation in mine wastes: An EXAFS spectroscopic study. *Appl. Geochem.* **2004**, *19* (3), 379−393.

(13) Moreno, T.; Oldroyd, A.; McDonald, I.; Gibbons, W. Preferential fractionation of trace metals-metalloids into PM10 resuspended from contaminated gold mine tailings at Rodalquilar, Spain. *Water Air Soil Pollut.* **2007**, *179* (1−4), 93−105.

(14) Moore, J. N.; Brook, E. J.; Johns, C. Grain-size partitioning of metals in contaminated, coarse-grained river floodplain sediment: Clark Fork River, Montana, United States. *Environ. Geol. Water Sci.* **1989**, *14* (2), 107−115.

(15) Harsh, J. B.; Doner, H. E. Characterization of mercury in a riverwash soil. *J. Environ. Qual.* **1981**, *10* (3), 333−337.

(16) Corriveau, M. C.; Jamieson, H. E.; Parsons, M. B.; Campbell, J. L.; Lanzirotti, A. Direct characterization of airborne particles associated with arsenic-rich mine tailings: Particle size, mineralogy and texture. *Appl. Geochem.* **2011**, *26* (9−10), 1639−1648.

(17) Singer, D. M.; Zachara, J. M.; Brown, G. E. Uranium speciation as a function of depth in contaminated Hanford sediments—A micro-XRF, micro-XRD, and micro- and bulk-XAFS study. *Environ. Sci. Technol.* **2009**, *43* (3), 630−636.

(18) Bernaus, A.; Gaona, X.; Esbri, J. M.; Higueras, P.; Falkenberg, G.; Valiente, M. Microprobe techniques for speciation analysis and geochemical characterization of mine environments: The mercury district of Almaden in Spain. *Environ. Sci. Technol.* **2006**, *40* (13), 4090−4095.

(19) Walker, S. R.; Jamieson, H. E.; Lanzirotti, A.; Andrade, C. F.; Hall, G. E. M. The speciation of arsenic in iron oxides in mine wastes from the Giant gold mine, NWT: Application of synchrotron micro-XRD and micro-XANES at the grain scale. *Can. Mineral.* **2005**, *43*, 1205−1224.

(20) Rytuba, J. J.; Kim, C. S.; Goldstein, D. N., Review of samples of tailings, soils and stream sediment adjacent to and downstream from the Ruth Mine, Inyo County, California. In U.S. Geological Survey Open-File Report 2011−1105: 2011; p 37.

(21) Rytuba, J. J.; Kim, C. S.; Goldstein, D. N., Review of samples of sediment, tailings, and waters adjacent to the Cactus Queen gold mine, Kern County, California. In U.S. Geological Survey Open-File Report 2011−1034: 2011; p 34.

(22) Webb, S. M. Microanalysis Toolkit. http://www-ssrl.slac.stanford.edu/~swebb/smak.htm

(23) Cances, B.; Juillot, F.; Morin, G.; Laperche, V.; Polya, D.; Vaughan, D. J.; Hazemann, J. L.; Proux, O.; Brown, G. E.; Calas, G. Changes in arsenic speciation through a contaminated soil profile: A XAS based study. *Sci. Total Environ.* **2008**, *397* (1−3), 178−189.

(24) Slowey, A. J.; Johnson, S. B.; Newville, M.; Brown, G. E. Speciation and colloid transport of arsenic from mine tailings. *Appl. Geochem.* **2007**, *22* (9), 1884−1898.

(25) Paktunc, D.; Foster, A.; Heald, S.; Laflamme, G. Speciation and characterization of arsenic in gold ores and cyanidation tailings using

X-ray absorption spectroscopy. *Geochim. Cosmochim. Acta* **2004**, *68* (5), 969−983.
(26) Foster, A. L.; Brown, G. E., Jr.; Tingle, T.; Parks, G. A. Quantitative arsenic speciation in mine tailings using X-ray absorption spectroscopy. *Am. Mineral.* **1998**, *83* (5−6), 553−568.
(27) Webb, S. M. SIXpack: a graphical user interface for XAS analysis using IFEFFIT. *Phys. Scr.* **2005**, *T115*, 1011−1014.
(28) Malinowski, E. R. *Factor Analysis in Chemistry*, 2nd ed.; Wiley & Sons, Inc.: New York, 1991; p 350.
(29) Ressler, T.; Wong, J.; Roos, J.; Smith, I. L. Quantitative speciation of Mn-bearing particulates emitted from autos burning (methylcyclopentadienyl)manganese tricarbonyl-added gasolines using XANES spectroscopy. *Environ. Sci. Technol.* **2000**, *34* (6), 950−958.
(30) Wang, S. L.; Mulligan, C. N. Speciation and surface structure of inorganic arsenic in solid phases: A review. *Environ. Int.* **2008**, *34* (6), 867−879.
(31) Kim, C. S.; Brown, G. E., Jr.; Rytuba, J. J. Characterization and speciation of mercury-bearing mine wastes using X-ray absorption spectroscopy (XAS). *Sci. Total Environ.* **2000**, *261* (1−3), 157−168.
(32) Ostergren, J. D.; Brown, G. E., Jr.; Parks, G. A.; Tingle, T. N. Quantitative speciation of lead in selected mine tailings from Leadville, CO. *Environ. Sci. Technol.* **1999**, *33* (10), 1627−1636.
(33) Rehr, J. J.; Leon, J. M. d.; Zabinsky, S. I.; Albers, R. C. Theoretical X-ray absorption fine-structure standards. *J. Am. Chem. Soc.* **1991**, *113* (14), 5135−5140.
(34) Corriveau, M. C.; Jamieson, H. E.; Parsons, M. B.; Hall, G. E. M. Mineralogical characterization of arsenic in gold mine tailings from three sites in Nova Scotia. *Geochem.-Explor. Environ. Anal.* **2011**, *11* (3), 179−192.
(35) Fawcett, S. E.; Jamieson, H. E. The distinction between ore processing and post-depositional transformation on the speciation of arsenic and antimony in mine waste and sediment. *Chem. Geol.* **2011**, *283* (3−4), 109−118.
(36) Drahota, P.; Rohovec, J.; Filippi, M.; Mihaljevic, M.; Rychlovsky, P.; Cerveny, V.; Pertold, Z. Mineralogical and geochemical controls of arsenic speciation and mobility under different redox conditions in soil, sediment and water at the Mokrsko-West gold deposit, Czech Republic. *Sci. Total Environ.* **2009**, *407* (10), 3372−3384.
(37) Filippi, M.; Dousova, B.; Machovic, V. Mineralogical speciation of arsenic in soils above the Mokrsko-west gold deposit, Czech Republic. *Geoderma* **2007**, *139* (1−2), 154−170.
(38) Committee on Medical and Biological Effects of Environmental Pollutants, N. R. C., *Arsenic: Medical and Biological Effects of Environmental Pollutants*; National Academy of Sciences: Washington, D.C., 1977; p 340.
(39) Paktunc, D.; Dutrizac, J.; Gertsman, V. Synthesis and phase transformations involving scorodite, ferric arsenate and arsenical ferrihydrite: Implications for arsenic mobility. *Geochim. Cosmochim. Acta* **2008**, *72* (11), 2649−2672.
(40) Lombi, E.; Sletten, R. S.; Wenzel, W. W. Sequentially extracted arsenic from different size fractions of contaminated soils. *Water Air Soil Pollut.* **2000**, *124* (3−4), 319−332.

SUPPORTING INFORMATION

(Micro)spectroscopic Analyses of Particle Size Dependence on Arsenic Distribution and Speciation in Mine Wastes

Kim, C.S.[1*], Chi, C.[1], Miller, S.R.[1], Rosales, R.A.[1], Sugihara, E.S.[1], Akau, J.[1], Rytuba, J.J.[2], and Webb, S.M.[3]

[1] School of Earth and Environmental Sciences, Schmid College of Science, Chapman University, One University Drive, Orange, CA 92866

[2]U.S. Geological Survey, 345 Middlefield Road, MS 901, Menlo Park, CA 94305

[3]Stanford Synchrotron Radiation Lightsource, 2575 Sand Hill Road, MS: 69, Menlo Park, CA 94025

*contact email: cskim@chapman.edu

Micro-X-ray diffraction (μXRD) analysis

Experimental Method

Micro-X-ray diffraction images were collected on selected As- and Fe-rich particles identified from the μXRF maps collected at beamline 13-ID-D of the Advanced Photon Source. For each map, between 3-5 As-rich and 3-5 Fe-rich particles were investigated using μXRD. Data was collected with a 5 μm x 5 μm beam spot size at 18keV onto a MAR165 CCD camera, with the sample-detector distance, beam center position, and other relevant parameters calibrated using a LaB_6 powder standard. Before each μXRD image collection, the beam position was optimized in order to maximize the count rate of As or Fe before collecting each pattern for 30 seconds. Where needed (every 3-5 samples), areas of very low diffraction counts were also imaged in order to obtain background patterns for later subtraction.

After μXRD collection, the software program FIT2D [1] was used to integrate the diffraction images, generating 2-D single-particle diffraction patterns which were then background-subtracted and analyzed using the software program JADE version 6.0 (Materials Data Inc., Livermore, CA) and compared against the ICSD Minerals database in order to identify the mineralogy of the individual particles.

Results and Discussion

A total of 9 different sample size fractions among the 4 samples studied was investigated using μXRD, with diffraction images collected on 27 As-rich particles and 31 Fe-rich particles. However, peak matching attempts of the resulting integrated diffraction patterns was only minimally successful for As phase identification, with just 2 of the 27 μXRD patterns (a 7% match rate) from As-rich particles matching conclusively with As-bearing minerals. The other diffraction patterns either failed to match with any phases in the ICSD mineral database or, more commonly, produced matches with minerals not known to contain substantial concentrations of arsenic, (quartz, lepidocrocite, nontronite, and muscovite) suggesting diffraction contributions from surrounding matrix minerals.

The two successful matches were identified as arseniosiderite, $Ca_3Fe_4^{+3}(AsO_4)_4(OH)_6 \bullet 3H_2O$, and scorodite, $FeAsO_4 \bullet 2H_2O$, both co-located with quartz, SiO_2 (**Figure S1**). Both phases are known and have been observed elsewhere to occur as secondary minerals formed by the oxidation of arsenopyrite or other arsenic-bearing species [2-4], which is consistent with the mineralogy of the ore deposit and the primary As-bearing minerals originally present. Notably, both As minerals identified through μXRD analysis contain Fe as part of their chemical composition, further supporting the correlation between the two elements noted in both the macroscopic and μXRF analyses. Additionally, despite the low match rate, any information

obtained on arsenic mineralogy through such microbeam methods is an improvement over bulk XRD techniques, which are incapable of producing such identification at the bulk concentrations present (only reaching as high as 0.8% arsenic by mass; typically at least 1-5% is needed to identify a mineral phase with bulk XRD).

Fitting of diffraction patterns collected from Fe-rich particles was more successful, yielding Fe-bearing phases in 14 out of 31 attempts (an effective match rate of 45%). Identified minerals included jarosite, ferrihydrite, goethite, and lepidocrocite, all common iron oxyhydroxide phases found in highly oxidized, weathered mine tailings. Two of these phases, ferrihydrite and goethite, were identified as substrates for As(V) adsorption in EXAFS linear combination fitting as detailed in the main text. However, as with the As-rich spots, the majority of diffraction patterns analyzed either could not be conclusively matched to a crystalline phase or yielded matrix minerals that do not typically contain iron, including quartz and clay minerals such as muscovite and illite.

Poor matches to μXRD diffraction patterns likely arise from 1) difficulties in background fitting and removal from the integrated patterns; 2) a beam-to-particle size ratio resulting in a high probability of single particle diffraction-based spots instead of powder diffraction-based rings, impacting relative peak intensity and the appearance of specific peaks; 3) the presence of amorphous, poorly-crystalline, or sorbed As- or Fe-bearing phases; and 4) the abundance of co-located, more highly-crystalline mineral phases whose strong diffraction swamp the relatively lower diffraction signal of the desired particles.

Although novel in its ability to provide mineralogical information with a high level of spatial resolution, this method as attempted in this study, in addition to having a low success rate, is highly non-representative and therefore a generally unreliable technique for consistently

determining the speciation of As- and Fe-rich particles in the samples investigated. Accordingly, no trends in speciation could be identified as a function of particle size or comparisons between tailings and background samples made using μXRD.

References

1. Hammersley, A. *FIT2D: an Introduction and Overview; Internal Report ESRF97HA02*; ESRF: Grenoble, France, 1997.
2. Dove, P. M.; Rimstidt, J. D., The solubility and stability of scorodite, FeAsO4.2H2O. *American Mineralogist* **1985,** *70*, (7-8), 838-844.
3. Drahota, P.; Rohovec, J.; Filippi, M.; Mihaljevic, M.; Rychlovsky, P.; Cerveny, V.; Pertold, Z., Mineralogical and geochemical controls of arsenic speciation and mobility under different redox conditions in soil, sediment and water at the Mokrsko-West gold deposit, Czech Republic. *Science of the Total Environment* **2009,** *407*, (10), 3372-3384.
4. Filippi, M.; Dousova, B.; Machovic, V., Mineralogical speciation of arsenic in soils above the Mokrsko-west gold deposit, Czech Republic. *Geoderma* **2007,** *139*, (1-2), 154-170.

SUPPORTING INFORMATION—FIGURE AND TABLE CAPTIONS

Figure S1. Peak matching results for micro-X-ray diffraction patterns of two different As-bearing particles, identified as a) arseniosiderite and b) scorodite (both co-located with quartz).

Figure S2. Arsenic and iron concentrations as a function of particle size in the Descarga background (D-BG) sample (a, b), Solomon Mine tailings (SM-MT) (c, d), and Solomon Mine background (SM-BG) sample (e, f), respectively. The average bulk concentration of each element in the sample is designated on the plots by a horizontal dotted gray line. Refer to Table 1 of the main text for a listing of the particle size ranges corresponding to each labeled size fraction S1-S11.

Figure S3-S5. μXRF maps of the a) S5 (250-500 μm), b) S7 (75-125 μm), c) S9 (32-45 μm), and d) S11 (≤20 μm) size fractions of the Descarga background (D-BG) sample, Solomon Mine tailings (SM-MT), and Solomon Mine background (SM-BG) sample. Arsenic Kα fluorescence is shown in red and iron Kα fluorescence is shown in blue. The maximum intensity threshold of both elements was scaled down by 50% in order to increase their brightness in the maps.

Figure S6-S8. Iron (x-axis) and arsenic (y-axis) correlation plots of size fractions a) S5 (250-500 μm), b) S7 (75-125 μm), c) S9 (32-45 μm), and d) S11 (≤20 μm) from the Descarga background (D-BG) sample, Solomon Mine tailings (SM-MT), and Solomon Mine background (SM-BG) sample. Units for both axes are the number of windowed fluorescence counts collected per 500 ms.

Figure S9-S12. Stacked EXAFS plots showing the raw data (black) and linear combination fits (red) for EXAFS spectra of each size fraction for the Descarga mine tailings (D-MT), Descarga background (D-BG) sample, Solomon Mine tailings (SM-MT), and Solomon Mine background (SM-BG) sample.

Table S1. Parameters for μXRF scan area and beam dimensions according to particle size, accommodating 150 particles and 70 data points per particle.

Table S2. EXAFS linear combination fitting results for selected size fractions from the Descarga mine tailings (D-MT), Descarga background (D-BG) sample, Solomon Mine tailings (SM-MT), and Solomon Mine background (SM-BG) sample.

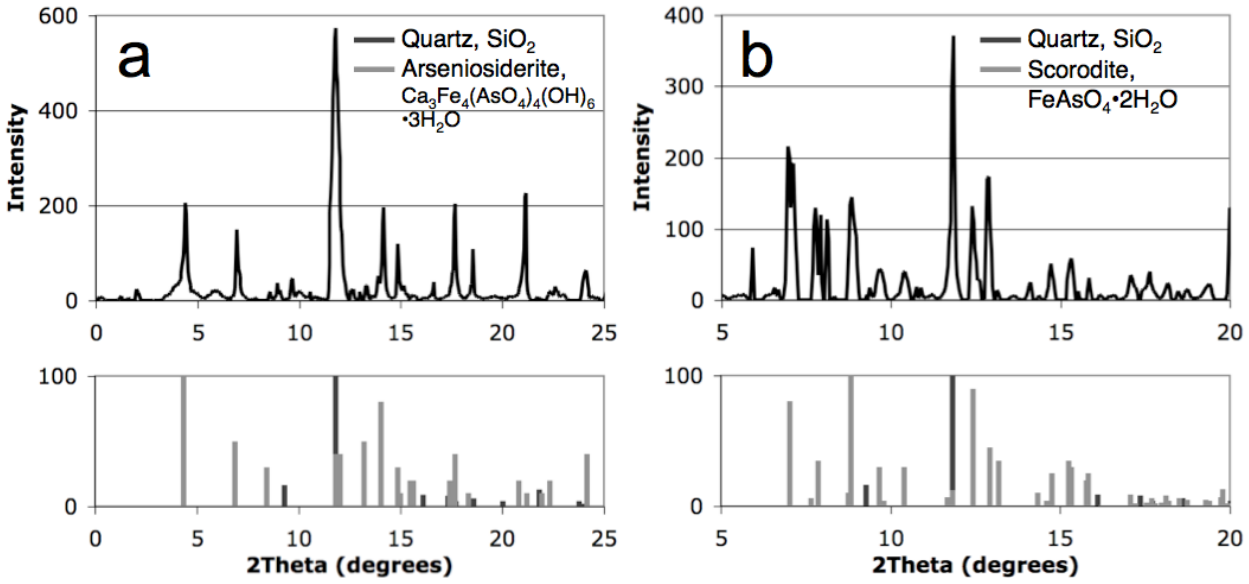
a
Quartz, SiO2
Arseniosiderite,
Ca3Fe4(AsO4)4(OH)6
•3H2O
Intensity
2Theta (degrees)
b
Quartz, SiO2
Scorodite,
FeAsO4•2H2O
Intensity
2Theta (degrees)

Figure S1.

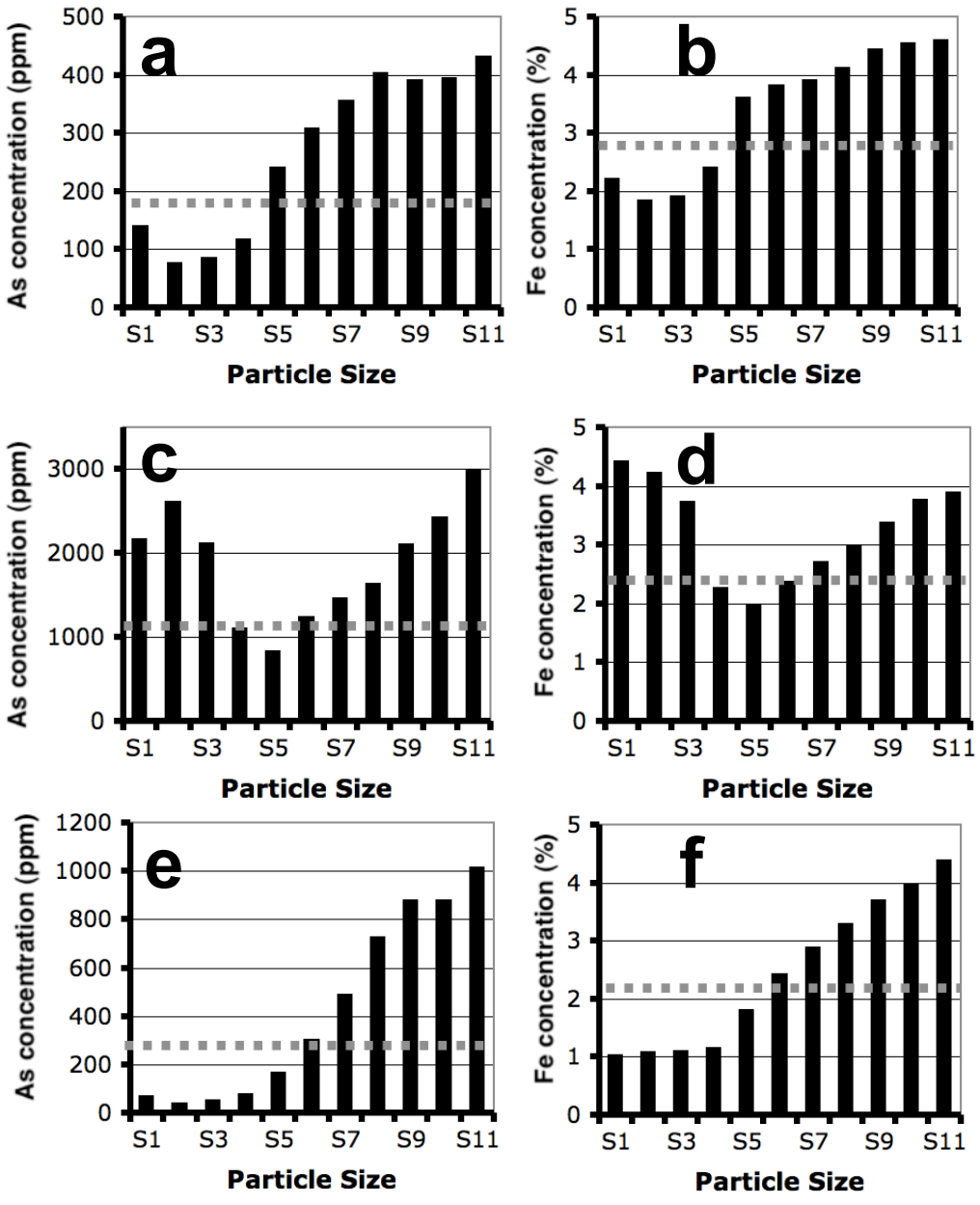
a
As concentration (ppm)
500
400
300
200
100
0
S1
S3
S5
S7
S9
S11
Particle Size
b
Fe concentration (%)
5
4
3
2
1
0
S1
S3
S5
S7
S9
S11
Particle Size
c
As concentration (ppm)
3000
2000
1000
0
S1
S3
S5
S7
S9
S11
Particle Size
d
Fe concentration (%)
5
4
3
2
1
0
S1
S3
S5
S7
S9
S11
Particle Size
e
As concentration (ppm)
1200
1000
800
600
400
200
0
S1
S3
S5
S7
S9
S11
Particle Size
f
Fe concentration (%)
5
4
3
2
1
0
S1
S3
S5
S7
S9
S11
Particle Size

Figure S2.

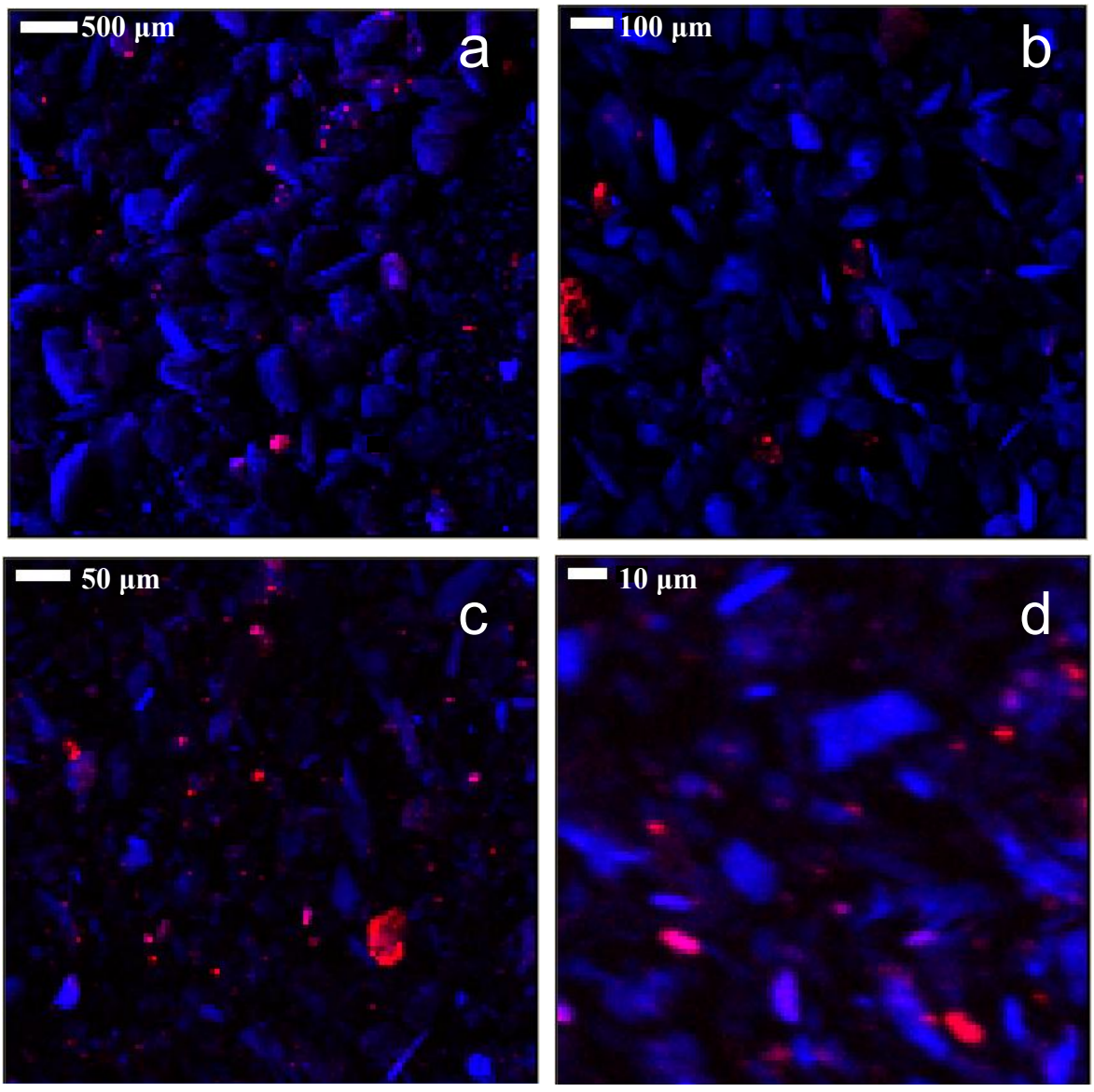

Figure S3.

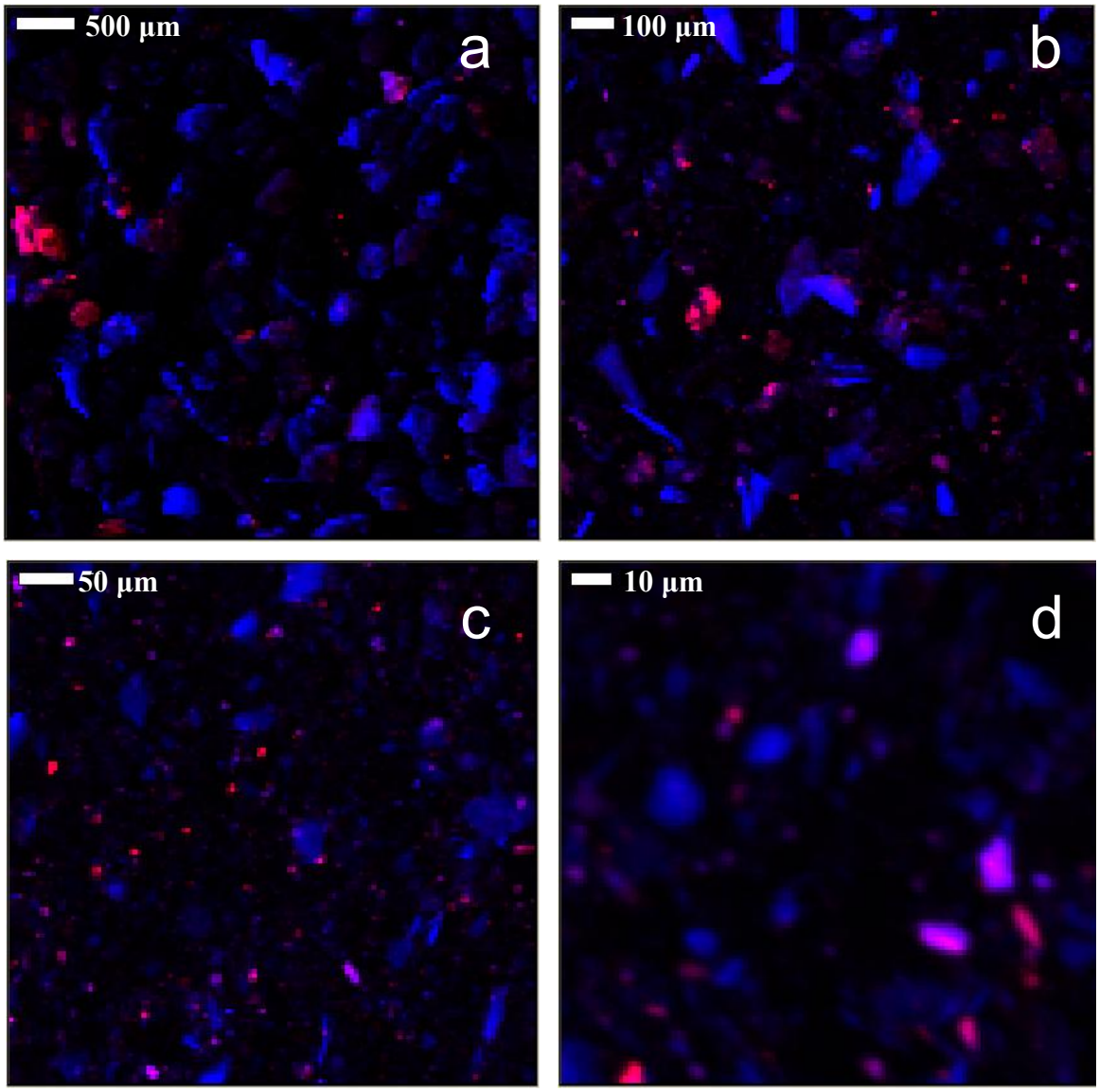

Figure S4.

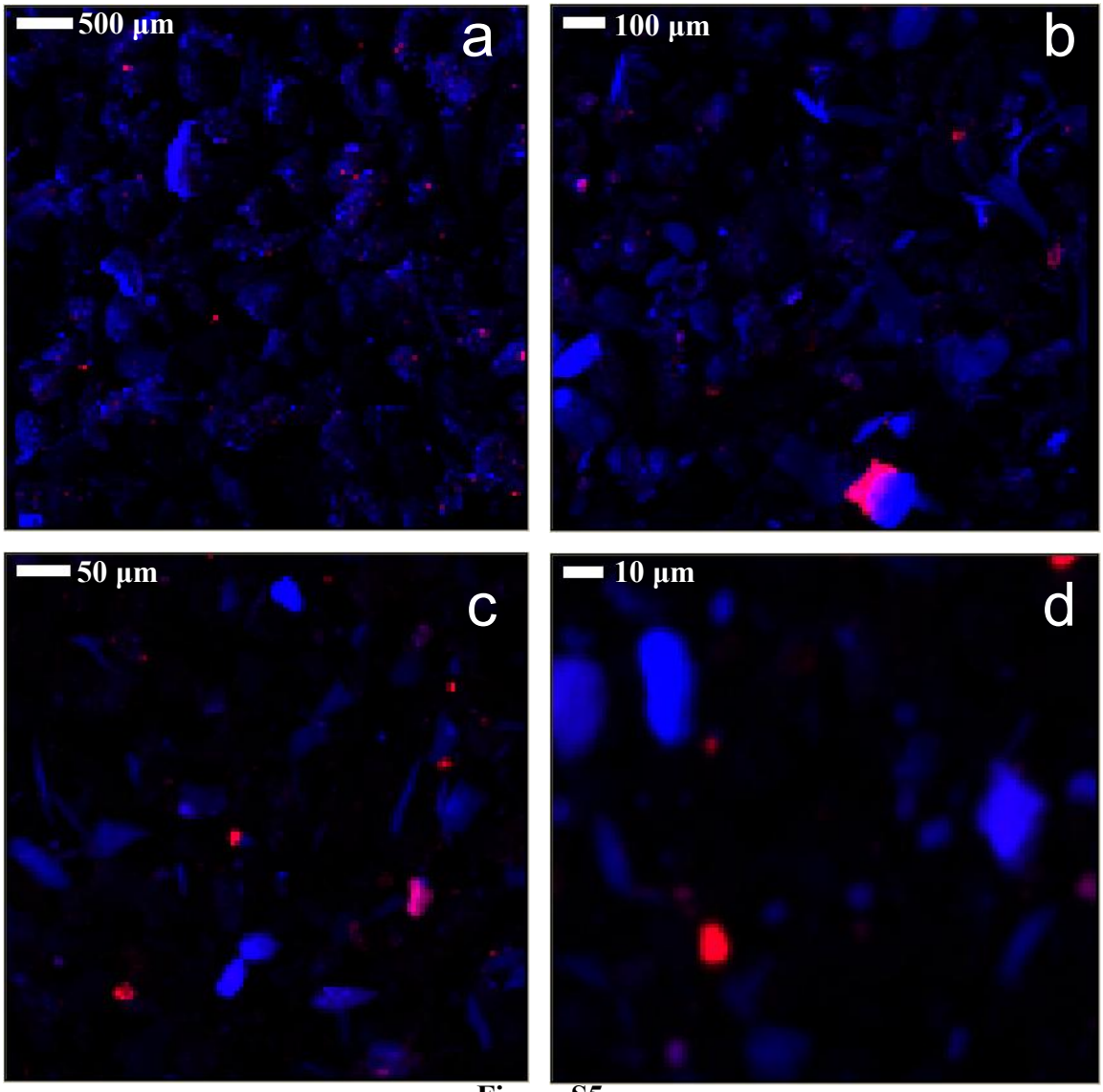

Figure S5.

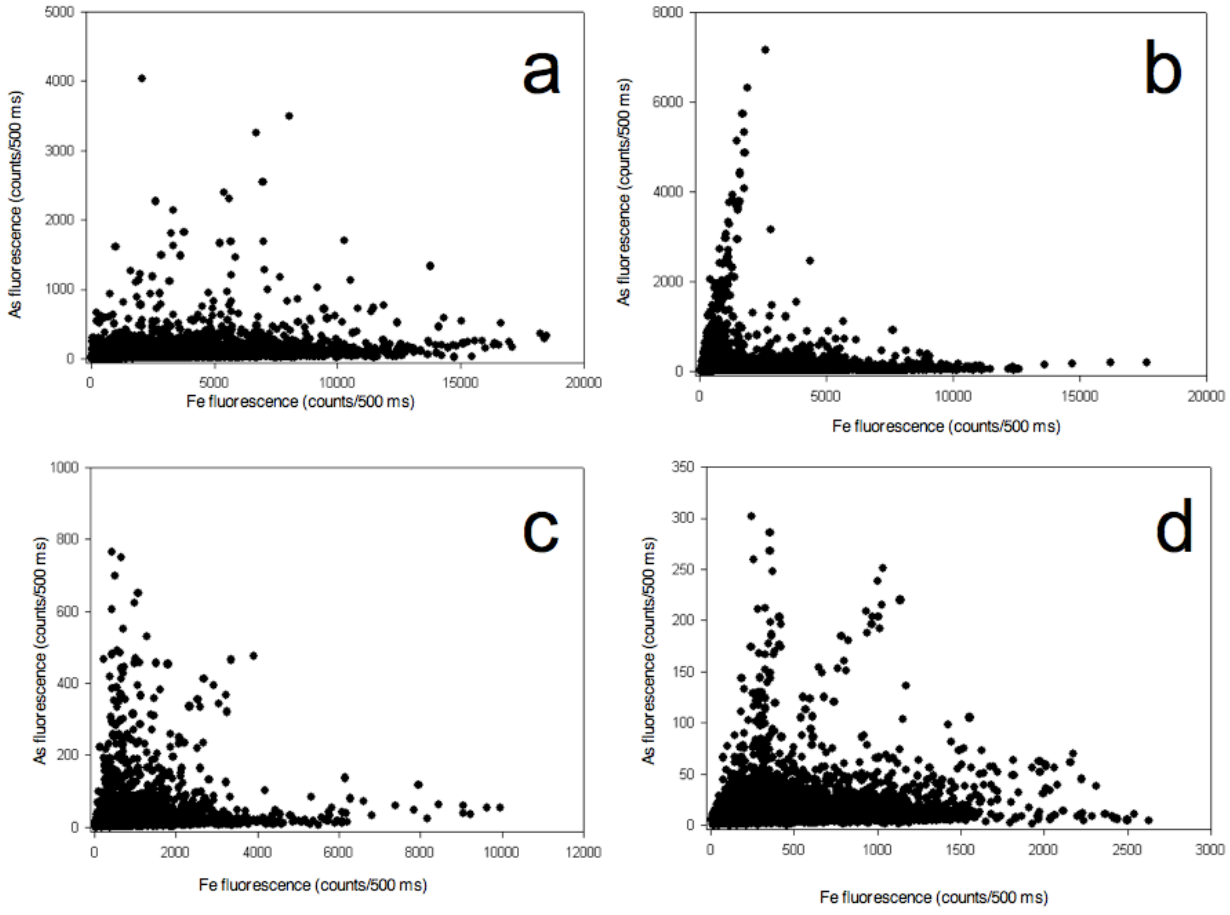
a
As fluorescence (counts/500 ms)
Fe fluorescence (counts/500 ms)
b
As fluorescence (cpunts/500 ms)
Fe fluorescence (counts/500 ms)
c
As fluorescence (counts/500 ms)
Fe fluorescence (counts/500 ms)
d
As fluorescence (counts/500 ms)
Fe fluorescence (counts/500 ms)

Figure S6.

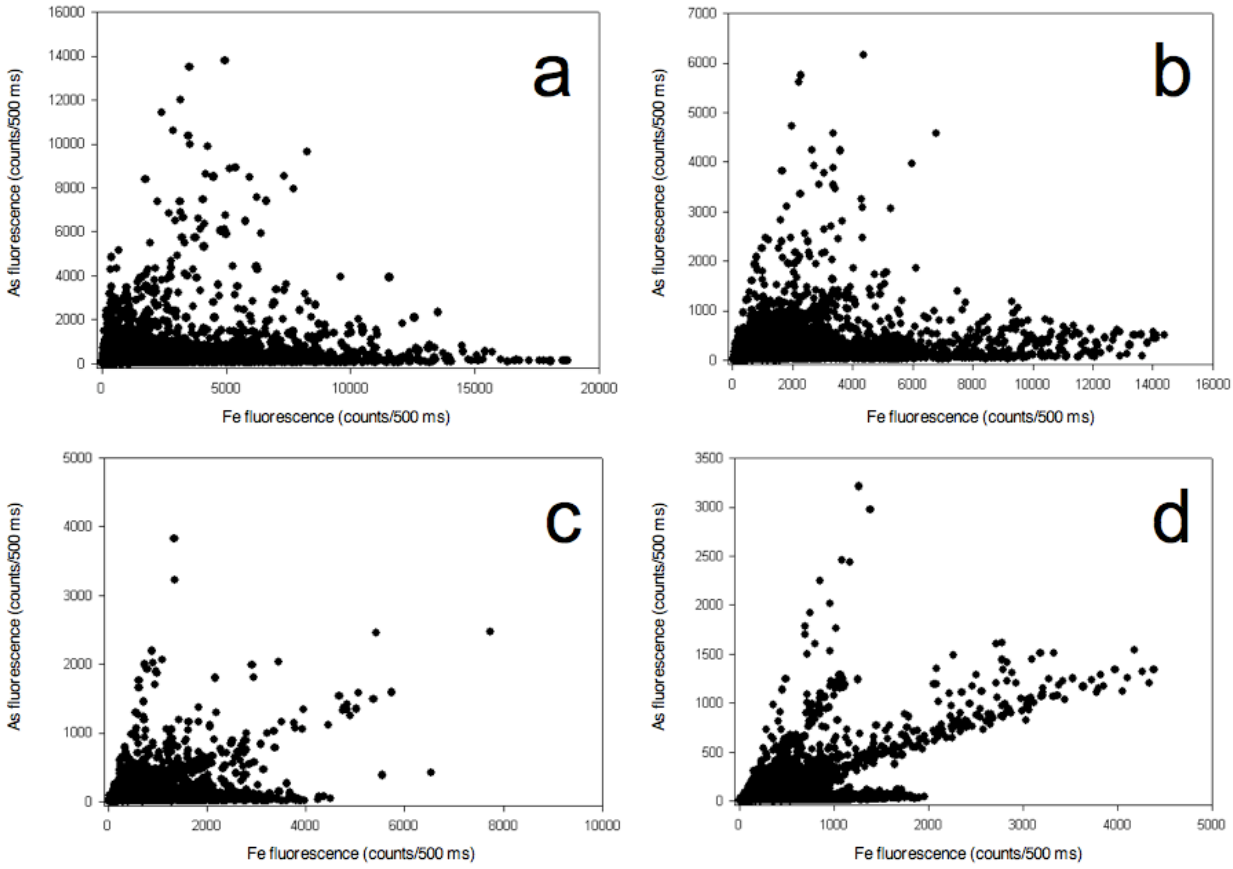
a
As fluorescence (counts/500 ms)
Fe fluorescence (counts/500 ms)
b
As fluorescence (counts/500 ms)
Fe fluorescence (counts/500 ms)
c
As fluorescence (counts/500 ms)
Fe fluorescence (counts/500 ms)
d
As fluorescence (counts/500 ms)
Fe fluorescence (counts/500 ms)

Figure S7.

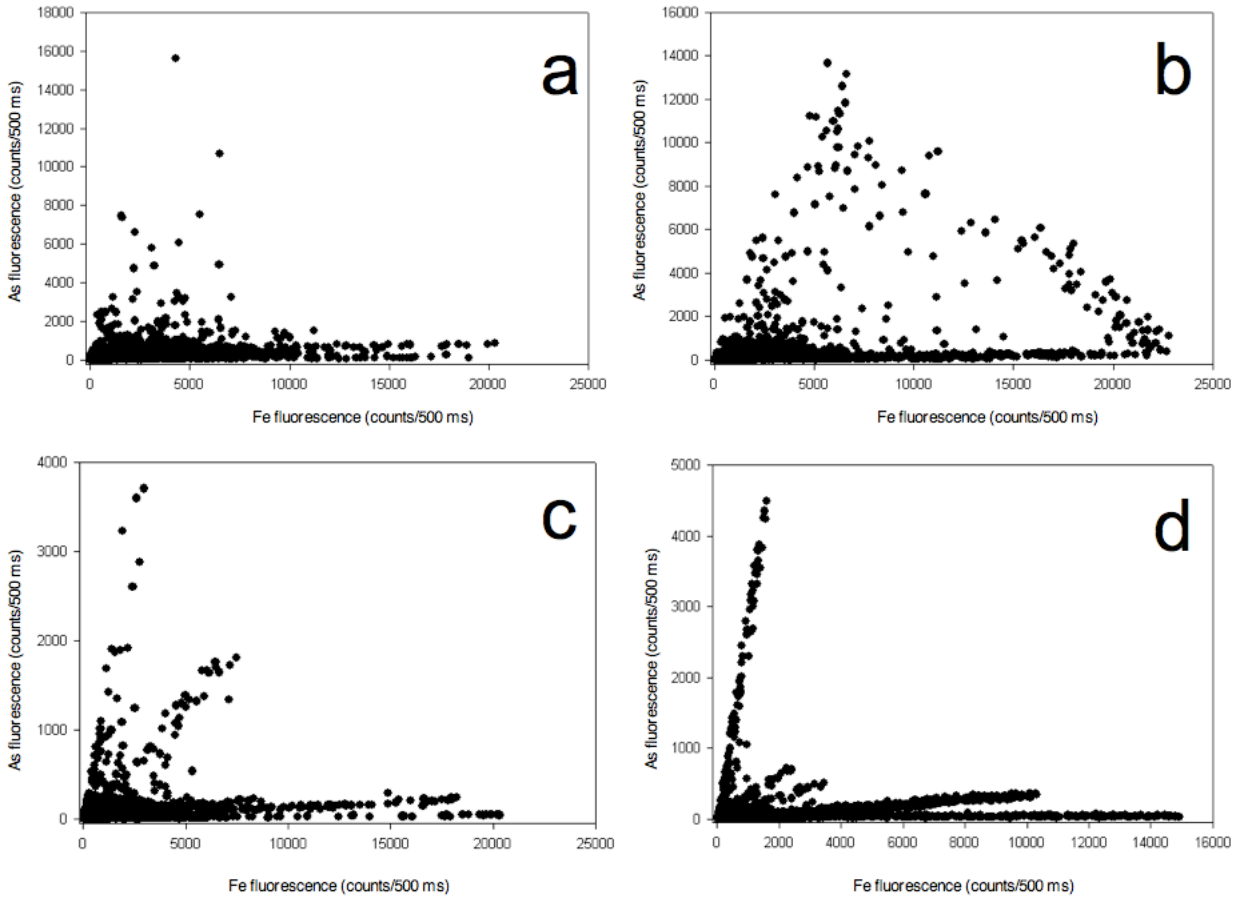
a
As fluorescence (counts/500 ms)
Fe fluorescence (counts/500 ms)
b
As fluorescence (counts/500 ms)
Fe fluorescence (counts/500 ms)
c
As fluorescence (counts/500 ms)
Fe fluorescence (counts/500 ms)
d
As fluorescence (counts/500 ms)
Fe fluorescence (counts/500 ms)

Figure S8.

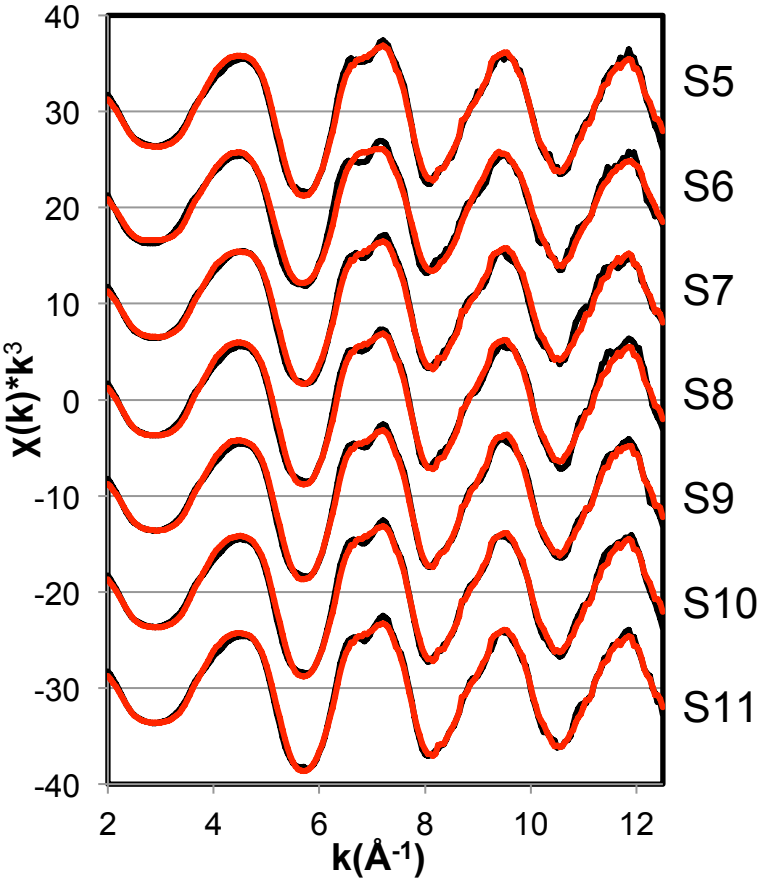

Figure S9.

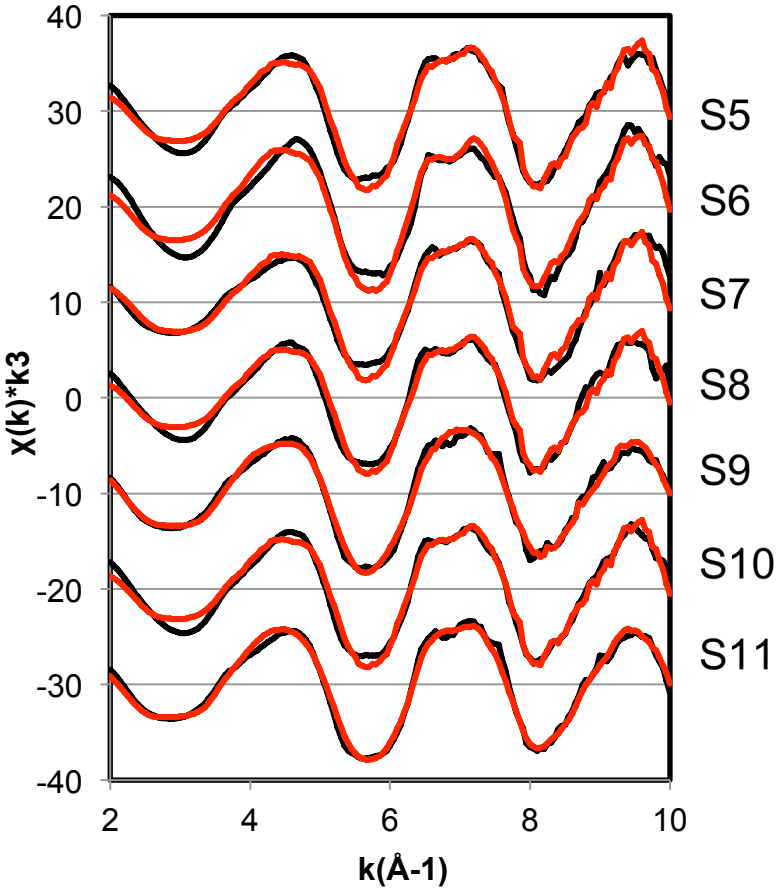

Figure S10.

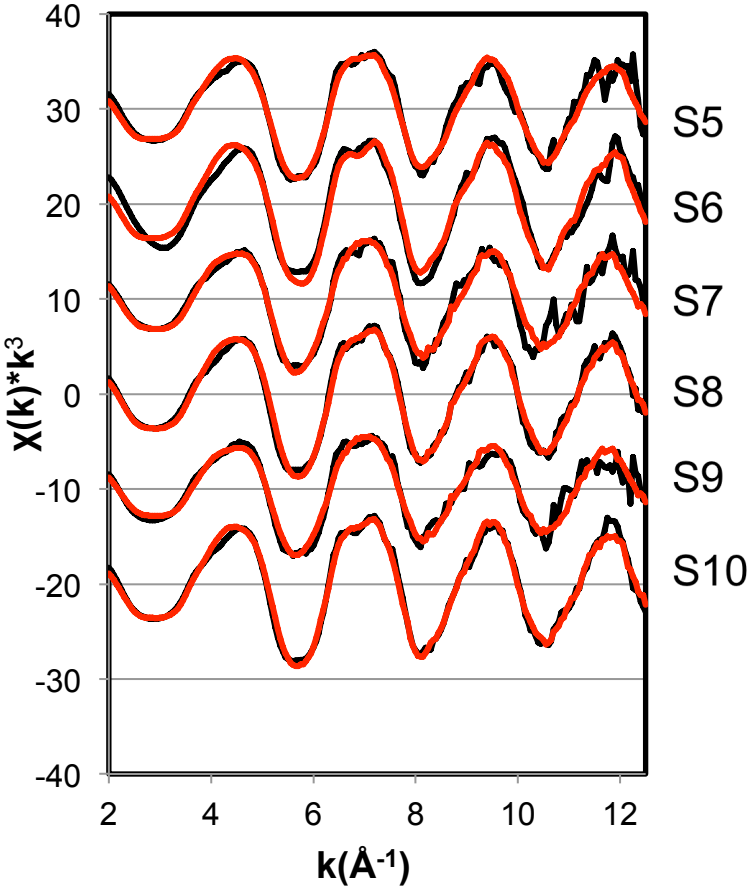

Figure S11.

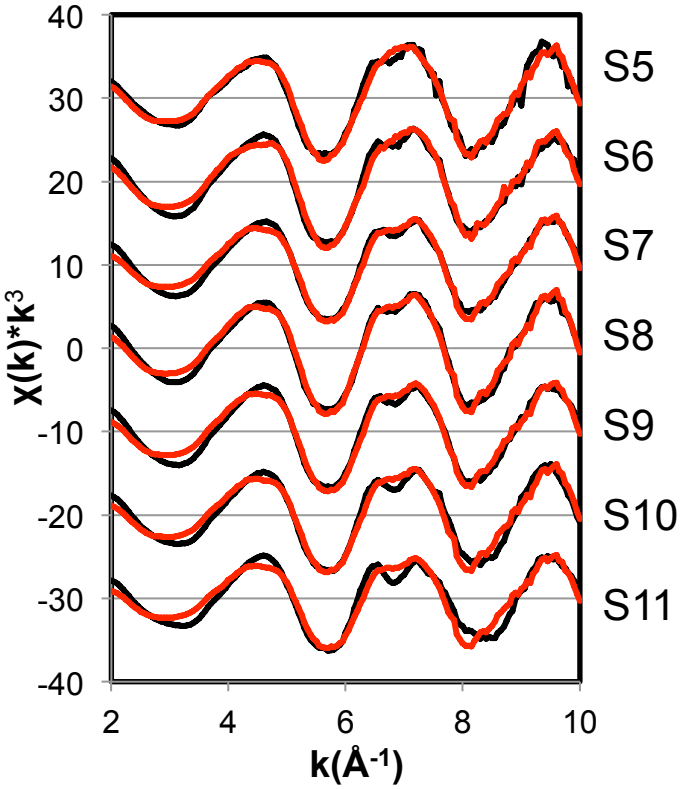

Figure S12.

Table S1.

Particle diameter range (mm)	Split	Length of scan area (mm)	Step size (mm)
250-500	S5	4560	54
75-125	S7	1220	15
32-45	S9	470	6
<20	S11	200	2.5

Table S2.

Sample (ID)	Size Fraction	As Conc. (ppm)	Sodium Arsenate, Na_2HAsO_4 (%)	Arseniosiderite, $Ca_2Fe_3(AsO_4)_3O_3 \cdot 3H_2O$ (%)	As(V) - ferrihydrite (%)	As(V) - goethite (%)	As(V) sorbed (%)	Total (%)	R Factor
D-MT	S5	2650	35	34	41	0	41	110	0.0167
	S6	3790	76	34	0	0	0	110	0.0211
	S7	3650	40	27	36	0	36	103	0.0177
	S8	4720	29	36	48	0	48	113	0.0199
	S9	7060	24	36	35	18	53	113	0.0094
	S10	8210	36	31	43	0	43	110	0.0155
	S11	N/A	35	32	41	0	41	108	0.0132
D-BG	S5	241	0	28	0	85	85	113	0.0255
	S6	307	0	60	0	60	60	120	0.0560
	S7	356	0	24	0	89	89	113	0.0394
	S8	402	0	35	0	74	74	109	0.0360
	S9	390	64	0	40	0	40	104	0.0158
	S10	394	0	35	0	78	78	113	0.0260
	S11	431	72	38	0	0	0	110	0.0133
SM-MT	S5	829	69	33	0	0	0	102	0.0442
	S6	1240	53	61	0	0	0	114	0.0497
	S7	1455	52	0	43	0	43	94	0.0654
	S8	1630	33	28	50	0	50	111	0.0182
	S9	2100	48	0	37	0	37	85	0.0571
	S10	2420	51	40	0	30	30	0	0.0172
SM-BG	S5	166	28	0	0	75	75	103	0.0309
	S6	301	0	0	54	39	93	93	0.0292
	S7	489	0	34	0	59	59	93	0.0281
	S8	726	0	33	0	76	76	108	0.0220
	S9	878	0	33	47	14	61	94	0.0394
	S10	879	0	28	0	66	66	94	0.0456
	S11	1015	0	31	0	51	51	82	0.0835